

A simple atmospheric model of the local and teleconnection responses to tropical heating anomalies

Sang-Ki Lee¹, Chunzai Wang² and Brian E. Mapes³

¹Cooperative Institute for Marine and Atmospheric Studies, University of Miami, Miami, FL

²Atlantic Oceanographic and Meteorological Laboratory, NOAA, Miami, FL

³Rosenstiel School of Marine and Atmospheric Sciences, University of Miami, Miami FL

2nd revision submitted to Journal of Climate
July 2008

Corresponding author address: Dr. Sang-Ki Lee, NOAA/AOML, 4301 Rickenbacker Causeway, Miami, FL 33149, USA. E-mail: Sang-Ki.Lee@noaa.gov.

ABSTRACT

A minimal complexity model of both the local and remote stationary responses of the atmosphere to tropical heating anomalies is described and demonstrated. Two levels are recast as baroclinic and barotropic components with thermal advection in the tropics neglected. The model is linearized about some idealized and realistic background wind fields and forced with a localized heating for illustration. In the tropics, the baroclinic responses are familiar from the Matsuno-Gill model; these excite barotropic responses by advective interactions with vertical background wind shear. The barotropic signals are in turn transmitted to high latitudes only in the presence of barotropic background westerly winds. For an El Niño like equatorial heating, the barotropic response has anticyclones to the north and south of the heating reinforcing (opposing) the anticyclonic (cyclonic) baroclinic gyres in the upper (lower) troposphere. With realistic background flows, the model reproduces the hemispheric asymmetry of ENSO teleconnections. Further experiments show that the winter hemisphere is favored mainly because the summer hemispheric subtropical jet is farther from the heating latitude, not because it is weaker, suggesting that the summer hemisphere can still host robust stationary Rossby waves if the heating occurs in the vicinity of the jet. As an example, we show that summer heating over the Atlantic warm pool (AWP) can have a profound impact on the summer climate of the North America and Europe.

1. Introduction

Originally developed by Matsuno (1966) and Gill (1980), the so-called Matsuno-Gill model is widely used and perhaps the simplest dynamic model for heat-induced tropical circulations of the atmosphere. Its simplicity stems from assuming a purely baroclinic vertical structure (Davey and Gill 1987), corresponding to a heat source (or sink) at the mid-troposphere. A heat source at the equator produces a damped Kelvin wave along the equator east of the heat source, and a damped Rossby wave that forms to the northwest and southwest of the heat source. These damped baroclinic Kelvin and Rossby waves depicted by the Matsuno-Gill model are the cornerstones for our understanding of heat-induced atmospheric circulations in the tropics.

However, the Matsuno-Gill model completely fails outside of the tropics. As demonstrated by Hoskins and Karoly (1981) and by Horel and Wallace (1981), a diabatic-heating anomaly associated with El Niño can also excite a stationary barotropic Rossby wave train (also referred to as heat-induced barotropic teleconnection pattern, or simply teleconnection in this paper), whose spatial pattern is somewhat similar to the intrinsic mode of mid-latitude variability known as the Pacific-North American (PNA) pattern (Lau 1981; Wallace and Gutzler 1981; Straus et al. 2007). As summarized in Klein et al (1999), the ENSO teleconnections cause significant climatic anomalies virtually all over the globe, notably the North Pacific Ocean, North America and the tropical North Atlantic Ocean. The limitation of the Matsuno-Gill model is clear because the ENSO teleconnection patterns are barotropic (or equivalent barotropic). Branstator (1983) showed that a non-divergent barotropic vorticity model linearized about a zonal jet is the simplest model for understanding the ENSO teleconnections. However, it is obvious that the barotropic vorticity model has no skill in simulating the ENSO-forced baroclinic response within

the tropics. Furthermore, the barotropic vorticity model alone cannot address properly the mechanisms involving the forcing of barotropic teleconnection patterns.

Multi-level models and even full atmospheric general circulation models (AGCMs) can be used to compute responses to heating with greater generality, but their complexity makes it difficult to gain insight into fundamental processes. This study describes an intermediate approach: a model of minimal complexity that can simulate both the heat-induced tropical response and its teleconnections to high latitudes. Specifically, we present a two-mode (barotropic and baroclinic) model that captures three fundamental dynamic processes: 1) a heat-induced baroclinic mode as described by the Matsuno-Gill model (Gill 1980); 2) a barotropic Rossby wave source that resulting from the conversion of the heat-induced baroclinic mode into barotropic anomalies; and 3) barotropic teleconnections to high latitudes as in the barotropic stationary wave model of Branstator (1983). In the following sections, we first derive the governing equations and discuss how the new model is distinguished from some of the previously used models. Then, after presenting the method of solution, we discuss the model solutions under some idealized and realistic background wind fields to better understand the effect of different basic states and also the mechanisms involving the generation of stationary barotropic Rossby wave patterns. Finally, some potential applications and limitations of the new model are discussed.

2. Description of the model equations and the method of solution

a. Model equations

The present model is a steady-state two-level (or two-mode) spherical-coordinate primitive equations model, linearized about a specified background flow. The governing equations for

such two-level model can be derived from the vector form of the horizontal momentum equation, which can be written as

$$\frac{\partial \mathbf{v}}{\partial t} + (\xi + f) \mathbf{k} \times \mathbf{v} = -\nabla \left(\phi + \frac{\mathbf{v} \cdot \mathbf{v}}{2} \right) - r\mathbf{v} + A\nabla^2 \mathbf{v}, \quad (1)$$

where \mathbf{v} is the horizontal wind vector; ξ is the relative vorticity; ϕ is the geopotential; f is the Coriolis parameter; r is the linear momentum damping coefficient; and A is the momentum diffusion coefficient. Note that vertical advection is neglected in (1). As noted in Robert (1966) and Bourke (1972), vectors such as horizontal wind fields have multiple values at the poles, thus (1) is not well suited for studying atmospheric motions on the globe. Therefore, as typically done in other global models, the horizontal wind fields are represented in terms of the vertical component of relative vorticity and the horizontal divergence. Thus, by taking the curl and divergence to (1), the equations for relative vorticity and horizontal divergence are obtained:

$$\frac{\partial}{\partial t} (\nabla^2 \psi) + \frac{1}{a \cos \theta} \left[\frac{\partial}{\partial \lambda} (u \nabla^2 \psi) + \frac{\partial}{\partial \theta} (\cos \theta v \nabla^2 \psi) \right] = -2\Omega \left(\sin \theta \nabla^2 \chi + \frac{v}{a} \right) - r \nabla^2 \psi + A \nabla^4 \psi, \quad (2)$$

$$\frac{\partial}{\partial t} (\nabla^2 \chi) - \frac{1}{a \cos \theta} \left[\frac{\partial}{\partial \lambda} (v \nabla^2 \psi) - \frac{\partial}{\partial \theta} (\cos \theta u \nabla^2 \psi) \right] = 2\Omega \left(\sin \theta \nabla^2 \psi - \frac{u}{a} \right) - \nabla^2 \left(\frac{u^2 + v^2}{2} + \phi \right) - r \nabla^2 \chi + A \nabla^4 \chi, \quad (3)$$

where λ and θ represent longitude and latitude, respectively, u and v denote the zonal and meridional flow components, respectively; ψ and χ denote the stream function and velocity potential, respectively; a is the radius of earth; and Ω is the rotational rate of the earth. The quantities u and v appearing in (2)-(3) are not prognostic variables but to be replaced using the following diagnostic relations:

$$u = -\frac{1}{a} \frac{\partial \psi}{\partial \theta} + \frac{1}{a \cos \theta} \frac{\partial \chi}{\partial \lambda}, \quad (4)$$

$$v = \frac{1}{a \cos \theta} \frac{\partial \psi}{\partial \lambda} + \frac{1}{a} \frac{\partial \chi}{\partial \theta}. \quad (5)$$

All dependent variables appearing in (2)-(5) are now separated into the background (or basic state) and anomaly components:

$$(\psi, \chi, \phi, u, v) = (\Psi, X, \Phi, U, V) + (\psi', \chi', \phi', u', v'). \quad (8)$$

Inserting (8) into (2)-(5) and ignoring products of primed terms, the linearized vorticity equation and divergence equation are obtained. After dropping the prime, this linearized vorticity equation becomes

$$\begin{aligned} \frac{\partial}{\partial t} (\nabla^2 \psi) + \frac{1}{a \cos \theta} \left[\frac{\partial}{\partial \lambda} (U \nabla^2 \psi + u \nabla^2 \Psi) + \frac{\partial}{\partial \theta} (\cos \theta V \nabla^2 \psi + \cos \theta v \nabla^2 \Psi) \right] + 2\Omega \left(\sin \theta \nabla^2 \chi + \frac{v}{a} \right) \\ = -r \nabla^2 \psi + A \nabla^4 \psi. \end{aligned} \quad (9)$$

Similarly, the linearized divergence equation becomes

$$\begin{aligned} \frac{\partial}{\partial t} (\nabla^2 \chi) - \frac{1}{a \cos \theta} \left[\frac{\partial}{\partial \lambda} (V \nabla^2 \psi + v \nabla^2 \Psi) - \frac{\partial}{\partial \theta} (\cos \theta U \nabla^2 \psi + \cos \theta u \nabla^2 \Psi) \right] - 2\Omega \left(\sin \theta \nabla^2 \psi - \frac{u}{a} \right) \\ + \nabla^2 (Uu + Vv + \phi) = -r \nabla^2 \chi + A \nabla^4 \chi. \end{aligned} \quad (10)$$

As mentioned earlier, the current model is designed to simulate a steady-state response of the atmosphere to heating anomalies. Thus, the time derivative terms appearing in (9)-(10) are dropped. Since the model atmosphere consists of two levels (centered at 250 mb and 750 mb), it is also convenient to separate the variables into the barotropic and baroclinic components:

$$\bar{Y} = 0.5(Y_1 + Y_2), \quad (11)$$

$$\hat{Y} = 0.5(Y_2 - Y_1), \quad (12)$$

where Y stands for ψ, χ and ϕ with subscripts 1 and 2 denoting values at the upper (250 mb) and lower (750 mb) levels, respectively. Note that the baroclinic components are defined in such a

way that their signs correspond to those at the lower level following the convention used in Gill (1980).

By adding the vorticity equation (9) of the upper and lower levels, we obtain the barotropic vorticity equation:

$$\begin{aligned} \frac{1}{a \cos \theta} \left[\frac{\partial}{\partial \lambda} (\bar{U} \nabla^2 \bar{\psi} + \bar{u} \nabla^2 \bar{\Psi}) + \frac{\partial}{\partial \theta} (\cos \theta \bar{V} \nabla^2 \bar{\psi} + \cos \theta \bar{v} \nabla^2 \bar{\Psi}) \right] + 2\Omega \frac{\bar{v}}{a} \\ = -r_0 \nabla^2 \bar{\psi} + A_0 \nabla^4 \bar{\psi} + F_{\bar{\psi}}, \end{aligned} \quad (13)$$

where r_0 is the linear momentum damping coefficient for barotropic motion; A_0 is the momentum diffusion coefficient for barotropic motion; and $F_{\bar{\psi}}$ represents the vorticity tendency terms that involve interactions between the vertical background shear and baroclinic wind anomalies:

$$F_{\bar{\psi}} = -\frac{1}{a \cos \theta} \left[\frac{\partial}{\partial \lambda} (\hat{U} \nabla^2 \hat{\psi} + \hat{u} \nabla^2 \hat{\Psi}) + \frac{\partial}{\partial \theta} (\cos \theta \hat{V} \nabla^2 \hat{\psi} + \cos \theta \hat{v} \nabla^2 \hat{\Psi}) \right]. \quad (14)$$

The vertically integrated (*i.e.*, barotropic) divergence is set to zero as in other simple models (Held and Suarez 1978; Schopf and Suarez 1988), and thus the associated term (*i.e.*, $2\Omega \sin \theta \nabla^2 \bar{\chi}$) disappears in (13).

Similarly, by subtracting the vorticity equation (9) of the upper level from that of the lower level, we obtain the baroclinic vorticity equation:

$$\begin{aligned} \frac{1}{a \cos \theta} \left[\frac{\partial}{\partial \lambda} (\bar{U} \nabla^2 \hat{\psi} + \hat{u} \nabla^2 \bar{\Psi}) + \frac{\partial}{\partial \theta} (\cos \theta \bar{V} \nabla^2 \hat{\psi} + \cos \theta \bar{v} \nabla^2 \bar{\Psi}) \right] + 2\Omega \left(\sin \theta \nabla^2 \hat{\chi} + \frac{\hat{v}}{a} \right) \\ = -r_1 \nabla^2 \hat{\psi} + A_1 \nabla^4 \hat{\psi} + F_{\hat{\psi}}, \end{aligned} \quad (15)$$

where r_1 is the linear momentum damping coefficient for baroclinic motion; and A_1 is the momentum diffusion coefficient for baroclinic motion; and $F_{\hat{\psi}}$ represents the vorticity tendency terms involving interactions between the vertical background wind shear and barotropic wind anomalies:

$$F_{\hat{\psi}} = -\frac{1}{a \cos \theta} \left[\frac{\partial}{\partial \lambda} (\hat{U} \nabla^2 \bar{\psi} + \bar{u} \nabla^2 \hat{\Psi}) + \frac{\partial}{\partial \theta} (\cos \theta \hat{V} \nabla^2 \bar{\psi} + \cos \theta \bar{v} \nabla^2 \hat{\Psi}) \right]. \quad (16)$$

Although the barotropic divergence is set to zero here, the baroclinic divergence cannot be neglected due to its importance over the tropics. Thus, the baroclinic divergence equation can be derived by subtracting the divergence equation (10) of the upper level from that of the lower level:

$$\begin{aligned} -\frac{1}{a \cos \theta} \left[\frac{\partial}{\partial \lambda} (\bar{V} \nabla^2 \hat{\psi} + \hat{v} \nabla^2 \bar{\Psi}) - \frac{\partial}{\partial \theta} (\cos \theta \bar{U} \nabla^2 \hat{\psi} + \cos \theta \hat{U} \nabla^2 \bar{\Psi}) \right] - 2\Omega \left(\sin \theta \nabla^2 \hat{\psi} - \frac{\hat{u}}{a} \right) \\ + \nabla^2 (\bar{U} \hat{u} + \bar{V} \hat{v} + \hat{\phi}) = -r_1 \nabla^2 \hat{\chi} + A_1 \nabla^4 \hat{\chi} + F_{\hat{\chi}}, \end{aligned} \quad (17)$$

where $F_{\hat{\chi}}$ represents the divergence tendency terms involving interactions between the vertical background wind shear and barotropic wind anomalies:

$$F_{\hat{\chi}} = \frac{1}{a \cos \theta} \left[\frac{\partial}{\partial \lambda} (\hat{V} \nabla^2 \bar{\psi} + \bar{v} \nabla^2 \hat{\Psi}) + \frac{\partial}{\partial \theta} (\cos \theta \hat{U} \nabla^2 \bar{\psi} + \cos \theta \bar{U} \nabla^2 \hat{\Psi}) \right] - \nabla^2 (\hat{U} \bar{u} + \hat{V} \bar{v}). \quad (18)$$

Finally, the equation for baroclinic geopotential ($\hat{\phi}$) can be written as

$$\gamma \hat{\phi} + c_g^2 \nabla^2 \hat{\chi} = -Q, \quad (19)$$

where γ is the thermal damping coefficient; c_g is the internal gravity wave speed; and Q is the diabatic heating rate. Note that (19) is in the same form as originally used in Gill (1980); thus, it can be derived by using continuity equation, hydrostatic equation, ideal gas law, and linearized thermodynamic equation. A detailed derivation of this equation is well documented in Kleeman (1989), thus it is not repeated here. Nevertheless, it is important to point out that in deriving (19), we use the so-called *weak temperature gradient approximation* - the terms involving the horizontal advection of baroclinic geopotential gradient (or mid-tropospheric temperature gradient) are neglected. Those terms include barotropic geopotential ($\bar{\phi}$), which never appears in

other equations. Therefore, by dropping those terms, we can also avoid complications arising from introducing an extra equation for $\bar{\phi}$. According to observational and modeling studies, the heat-induced teleconnection patterns are largely barotropic, while the baroclinic response is largely limited within the tropics (*e.g.*, Hoskins and Karoly 1981; Wallace and Gutzler 1981). Therefore, the fact that the simplified thermodynamic equation (19) is known to be very effective for the heat-induced baroclinic motion in the tropics (*e.g.*, Neelin 1988) justifies the using of (19) instead of more complex forms.

Specifying the basic states and the heating anomaly, (13)-(19) are in a closed form (note that $\bar{u}, \bar{v}(\hat{u}, \hat{v})$ are expressed in terms of $\bar{\psi}(\hat{\psi}, \hat{\chi})$ via (4)-(5)). In the next section, we present a numerical method to solve the governing equations (13)-(19).

Before we move on, it is useful to discuss how our model is distinguished from other simple and intermediate complexity models. One of these is the model developed by Wang and Li (1993) for modeling the annual cycle and short-term climate fluctuations in the tropics. Zebiak (1986) and Davey and Gill (1987) also expanded the Matsuno-Gill model by considering low-level moisture convergence, and by explicitly solving a moisture budget equation, respectively. However, none of these tropical models (based on Matsuno-Gill type dynamics) can reproduce the ENSO teleconnections to high latitudes. Perhaps the closest relative of the current model is the multi-level linear baroclinic model (LBM) used by Hoskins and Simmons (1975) and others (*e.g.*, Webster 1981; Kasahara and da Silva Dias 1986; Branstator 1990; Ting and Held 1990; Jin and Hoskins 1995; Watanabe and Kimoto 2000; Watanabe and Jin 2004). Although its complexity varies in different model versions, the LBM is virtually an AGCM, but linearized about observed (or idealized) basic states. In that sense, our model may be referred to as a stripped-down version of the dry LBM (Watanabe and Kimoto 2000). In particular, the

simplified thermodynamic equation (19) is the main component that distinguishes our model from other more complex LBMs.

b. Method of solution

The numerical method used to solve the governing equations (13)-(19) is similar to the technique used by Branstator (1983). More specifically, the heating anomaly Q and the prognostic variables $\bar{\psi}$, $\hat{\psi}$, $\hat{\chi}$, and $\hat{\phi}$ appearing in (13)-(19) are expressed as truncated series of spherical harmonics:

$$Y = \sum_{m=-M}^M \sum_{n=|m|}^N Y_n^m P_n^m(\theta) e^{im\lambda}, \quad (20)$$

where Y stands for $\bar{\psi}$, $\hat{\psi}$, $\hat{\chi}$, $\hat{\phi}$ and Q ; and P_n^m is the associated Legendre function. Inserting (20) into (13)-(19), multiplying by a complex conjugate spherical harmonic, $P_{n'}^{m'} e^{-im'\lambda}$, and integrating over the globe yield a set of linear equations, which can be solved by using a standard Gaussian elimination algorithm. The basic state variables, such as $\bar{\Psi}$ and $\hat{\Psi}$, and their derivatives are taken by representing them with the same form as in (20), and the associated integrals are evaluated using Gaussian quadrature. In order to calculate the matrix elements of the governing equations, we use the SPHEREPACK 3.0 (Adams and Swarztrauber 1999) to evaluate the spherical harmonics. For all cases in this paper, we use triangular 18 truncations or simply T18 (*i.e.*, $M=N=18$), but we find that T14 is quite sufficient for all the cases. For more details on the solution method, see Grose and Hoskins (1979) and Branstator (1983).

3. Some model experiments with idealized basic states

In this section, as a reference for understanding experiments with more realistic basic states, we first investigate how the new model simulates the local and teleconnection responses to a tropical heating anomaly under some idealized basic states. For all experiments, the internal gravity wave speed, c_g , is set to 60 ms^{-1} , which is a typical value used in previous studies (Kleeman 1989; Zebiak 1986). The thermal damping coefficient, γ , is set to $(2 \text{ days})^{-1}$ following Gill (1980), while the barotropic and baroclinic horizontal mixing coefficients, A_0 and A_1 , are both set to $10^6 \text{ m}^2 \text{ s}^{-1}$. The two linear momentum damping coefficients, r_0 and r_1 , are set to $(20 \text{ days})^{-1}$ and to $(10 \text{ days})^{-1}$, respectively. Neelin (1988) and Lin et al. (2008) discuss how different choices of the three baroclinic parameters, c_g , r_1 and γ affect the solution of the Matuno-Gill model.

We first consider a case with zero background flow (Case-1: $\bar{U} = \hat{U} = \bar{V} = \hat{V} = 0$). In this case, the barotropic vorticity equation (13) is decoupled from other three equations because the interactions between the vertical background wind shear and baroclinic wind anomalies are not allowed (*i.e.*, $F_{\bar{v}} = 0$ in (14)), thus the barotropic motion is not forced. Accordingly, the governing equations of the model are reduced to a special case of the Matuno-Gill model:

$$2\Omega \left(\sin \theta \nabla^2 \hat{\chi} + \frac{\hat{v}}{a} \right) = -r_1 \nabla^2 \hat{\psi} + A_1 \nabla^4 \hat{\psi}, \quad (21)$$

$$-2\Omega \left(\sin \theta \nabla^2 \hat{\psi} - \frac{\hat{u}}{a} \right) = -r_1 \nabla^2 \hat{\chi} + A_1 \nabla^4 \hat{\chi}, \quad (22)$$

$$\gamma \hat{\phi} + c_g^2 \nabla^2 \hat{\chi} = -Q, \quad (23)$$

where \hat{u} and \hat{v} are to be expressed in terms of $\hat{\psi}$ and $\hat{\chi}$ using (4) and (5). In the next example, we use a purely barotropic background flow of longitudinally invariant solid body rotation

(Case-2: $\bar{U} = \bar{U}_o \cos \theta$; $\hat{U} = \bar{V} = \hat{V} = 0$) with its maximum speed set to $\bar{U}_o = 25 \text{ ms}^{-1}$. By inspecting (13) and (14), it becomes obvious that the barotropic vorticity equation is still decoupled from the rest of equations as in the zero background flow case (Case-1). The only way to excite the barotropic motion is through the interactions between the vertical background shear and baroclinic wind anomalies (i.e., $F_{\bar{\psi}} \neq 0$ in (14)). Therefore, we can conclude that the vertical background wind shear is a critical factor that determines the amplitude of teleconnection to high latitudes, consistent with Kasahara and Silva Dias (1986) and Wang and Xie (1996). Consequently, the next case is a purely baroclinic background flow of longitudinally invariant solid body rotation (Case-3: $\hat{U} = \hat{U}_o \cos \theta$; $\bar{U} = \bar{V} = \hat{V} = 0$) with its maximum speed of $\hat{U}_o = 15 \text{ ms}^{-1}$. In this case, some barotropic motions can be excited in the tropics. However, we shall see that the barotropic vorticity source ($F_{\bar{\psi}}$) is merely balanced by Coriolis and damping terms such that the response is largely confined in the tropics near the heating. Finally, the next case is more like the real atmosphere where both the barotropic and baroclinic mean flow components exist (Case-4: $\bar{U} = \bar{U}_o \cos \theta$; $\hat{U} = \hat{U}_o \cos \theta$; $\bar{V} = \hat{V} = 0$) where $\bar{U}_o = 25 \text{ ms}^{-1}$ and $\hat{U}_o = 15 \text{ ms}^{-1}$. The values for \bar{U}_o and \hat{U}_o are chosen to mimic the winter hemisphere, with typical mean wind speeds of 40 ms^{-1} and 10 ms^{-1} for the upper and lower troposphere, respectively (e.g., Pexoto and Oort 1992). The details of the four experiments are summarized in Table 1.

In all four cases considered, a Gaussian-shaped heating anomaly is prescribed at the equator roughly corresponding to the heating anomaly associated with El Niño:

$$Q = Q_o \exp \left[- \left(\frac{\theta}{L_\theta} \right)^2 \right] \exp \left[- \left(\frac{\lambda - \lambda_o}{L_\lambda} \right)^2 \right], \quad (24)$$

where $\lambda_0 = 160^\circ\text{W}$, $L_\lambda = 25^\circ$, and $L_\theta = 5^\circ$. Q_0 is set equal to $2.5 \times 10^{-2} \text{ W kg}^{-1}$, which is equivalent to 2.15 K day^{-1} . Some numerical problems may arise when the spectral harmonics are used to represent fields with sharp spatial gradients such as (24). These problems, known as Gibbs oscillations, produce small amplitude ripple patterns in the vicinity of the Gaussian-shaped heating source. In order to suppress the Gibbs oscillations, a 2D isotropic filter is applied to the spherical harmonic form of (24) as suggested by Navarra et al (1994).

Figure 1 shows the baroclinic geopotential and wind (vector plot) anomalies for (a) Case-1 and (b) Case-2. Similarly, Fig. 2 shows the rotational components (baroclinic stream function and rotational wind anomalies), whereas Fig. 3 shows the divergent components (baroclinic velocity potential and divergent wind anomalies). Comparing the two cases, we find that an inclusion of the barotropic background wind (Case-2) modifies the Matsuno-Gill response (Case-1) in such a way that the damped Rossby wave nodes are shifted significantly to the east (i.e., in the downstream direction). The Rossby gyres are now directly to the north and south of the equatorial heating source, which is centered at 160°W . The eastward shift of the baroclinic anomalies in Case-2 can be thought as a Doppler shift via the barotropic background westerly wind. Other noticeable changes include a slight weakening of the divergent flow component (Fig. 3b), and a strengthening of the off-equatorial cyclonic vortex pair (Fig. 2b). However, the mechanism that triggers the barotropic flow anomalies is still missing in Case-2 (i.e., $F_{\bar{\psi}} = 0$ in (14)), thus the core dynamics of the heat-induced flow anomalies under the influence of the purely barotropic background flow are still governed by the original Matsuno-Gill model (Case-1).

The baroclinic components of the solution for Case-3 and Case-4 are very similar to those for Case-1 and Case-2, respectively (not shown). In other words, baroclinic background - barotropic anomaly interactions (i.e., $F_{\hat{\psi}}$ and $F_{\hat{\chi}}$ in (15) and (17)) have little impact on the baroclinic response. Furthermore, the differences between Cases-1 and -2 (and between Case-3 and -4, not shown) are small, compared to the large differences in the barotropic part we shall see below, indicating that the baroclinic impacts of barotropic background - baroclinic anomaly interactions (i.e., advection terms in the LHS of (15) and (17)) are also fairly weak. Therefore, we can conclude that even in the presence of moderate background flow the original Matsuno-Gill model (see (21)-(23)) still mainly governs the heat-induced baroclinic vorticity and divergence anomalies.

In contrast to these weak background effects on the baroclinic part of the response, the barotropic part is profoundly impacted by background-anomaly interactions. Figure 4 shows the barotropic components of stream function and rotational wind (vector plot) anomalies for (a) Case-3 and (b) Case-4. In both cases, the vertical background shear - baroclinic anomaly interactions ($F_{\bar{\psi}}$) play a very important role of forcing the barotropic motion near the heat source. It is also apparent that the barotropic response is to form an anticyclonic vortex pair to the north and south of the heating source. Since the baroclinic response has a cyclonic vortex pair in the same location (see Fig. 2a), the cyclonic vortex pair in the lower level is weakened, while the anticyclonic vortex pair in the upper level is strengthened as shown in Fig. 5 for Case-3 (see (12) for our sign convention). This is quite an interesting result because this tendency of the more (less) organized response in the upper (lower) troposphere during a typical El Niño has been recognized for quite some time but without any clear dynamic explanation.

With no barotropic background flow (Case-3), the forcing terms ($F_{\bar{\psi}}$) in (13) must be locally balanced by Coriolis and damping terms, because all four advection terms in the LHS of (13) are zero; thus, the barotropic anomalies are largely confined within the tropics near the heating source in Fig. 4a. In Case-4, on the other hand, the barotropic anomalies are transmitted to high latitudes (Fig. 4b) because terms involving the barotropic background wind - barotropic anomaly interactions (i.e., four advection terms in the LHS of (13)) permit a barotropic stationary Rossby wave solution. Therefore, the net conclusion is that both the barotropic and baroclinic background wind fields are required to radiate barotropic teleconnections to high latitudes. To some extents, the barotropic flow pattern shown in Fig. 4b has some similarity to the ENSO teleconnection patterns in boreal winter (Wallace and Gutzler 1981).

A commonly used interpretation for the difference between the Case-3 and Case-4 (Fig. 4) is that since barotropic Rossby waves have westward intrinsic phase velocities, a steady forcing in a resting barotropic background state cannot stimulate stationary barotropic Rossby waves - a westerly background flow is needed to balance the intrinsic phase velocity (e.g., Holton 1992). This can be easily demonstrated by using the dispersion relationship for barotropic Rossby wave in an infinite domain (e.g., Holton 1992):

$$\bar{c} = \bar{U}_o - \frac{\beta}{k^2 + l^2}, \quad (25)$$

where \bar{c} is the phase speed of barotropic Rossby wave, \bar{U} is barotropic background wind speed, β is the northward gradient of the vertical planetary vorticity, and k and l are zonal and meridional wave numbers, respectively. This equation clearly shows that $\bar{U} > 0$ in order for a

stationary barotropic waves to exist (i.e., $\bar{c} = 0$). We can also learn from this equation that the wavelength of barotropic stationary Rossby wave should increase as \bar{U} increases.

A natural next question is why there are no baroclinic teleconnections to high latitudes in our model (see Fig. 2b). The dispersion relationship for baroclinic Rossby wave (e.g., Holton 1992) can be written as

$$\hat{c} = \bar{U}_o - \frac{\beta}{k^2 + l^2 + 2R_d^{-2}}, \quad (26)$$

where \hat{c} is the phase speed of baroclinic Rossby wave and R_d is the baroclinic Rossby deformation radius. A stationary baroclinic Rossby wave can exist only if $0 < \bar{U} < 0.5\beta R_d^2$. Using typical values of $\beta = 2 \times 10^{-11} \text{ m}^{-1} \text{ s}^{-1}$ and $R_d = 10^3 \text{ km}$ in the mid-latitude ($\sim 30^\circ$), the critical barotropic background flow speed is about 9.9 ms^{-1} . Since the typical value for \bar{U} in the mid-latitude is about $15 \sim 30 \text{ ms}^{-1}$, we can argue that baroclinic Rossby waves propagate too slowly to become stationary in the mid-latitude.

Some sensitivity experiments were performed for Case-4 using different values for the five tunable damping coefficients, namely r_0 , A_0 , r_1 , A_1 and γ . For reasonable ranges of these values, reducing r_0 increases the amplitude of barotropic solution monotonically without affecting the baroclinic solution. But, when r_1 is reduced, both the baroclinic and barotropic solution components are amplified. These results are consistent with our findings that the heat-induced baroclinic motion, through its interactions with the vertical background shear, forces the barotropic motion, but the feedback from the barotropic to baroclinic motion is not significant. Additionally, when γ is decreased from $(2 \text{ days})^{-1}$ to $(10 \text{ days})^{-1}$, the baroclinic flow anomalies

tend to become more intense and to affect broader areas, but the overall structure of model solution remains unchanged consistent with Neelin (1988).

4. Further experiments with realistic basic states

Although the four experiments in the previous section provide some useful insights for the mechanisms of the local and teleconnection responses to tropical heating anomalies, the solid body rotation used as the basic state in those experiments is far from being realistic. Therefore, in this section, we use our model to further explore how realistic basic states affect the ENSO teleconnections to high latitudes. Fig. 6 shows the zonally averaged basic states for December-February (DJF) and June-August (JJA) obtained by using the stream functions at 250 and 750mb from the monthly NCAR-NCEP reanalysis (Kalnay et al. 1996). The basic states are zonally averaged only for the longitude band of 120°E - 100°W to focus on the ENSO teleconnections over the Pacific regions.

As summarized in Table 2, two model experiments are carried out using the zonally averaged basic states for DJF (Case-5) and JJA (Case-6) while keeping the model parameter values and the heating anomaly identical to the previous experiments. Fig. 7 shows the barotropic stream function and rotational wind anomalies for (a) Case-5 and (b) Case-6. The model solutions for these two cases are very different from those of the previous experiments in which a solid body rotation is used as the basic states. In particular, it is clear that the observed basic states (zonally averaged) can host robust ENSO teleconnections in the winter hemisphere, but not in the summer hemisphere.

The subtropical jet is more intense in the winter hemisphere than in the summer hemisphere (e.g., Peixoto and Oort 1992) as are both the vertical shear and the barotropic component of background wind (Fig. 6). It was shown above that barotropic wind anomalies near the heating source depend on vertical background shear, while the radiation of barotropic signals to high latitudes requires barotropic background flow. Therefore, one may argue that the vertical shear and barotropic wind of the subtropical jet in the summer hemisphere are too weak to produce robust ENSO teleconnections into the summer hemisphere (Webster 1981).

In addition, however, the subtropical jet *location* differs between hemispheres: the core is around 30° latitude in the winter hemisphere, and 45° in the summer hemisphere (Peixoto and Oort 1992). Therefore, both the vertical shear and barotropic background wind have their maxima migrating within the latitude band of $30^\circ - 45^\circ$ as shown in Fig. 6. Since the ENSO-induced baroclinic anomalies are largely confined within $30^\circ\text{S}-30^\circ\text{N}$ regardless of season summer-hemisphere baroclinic anomalies don't overlap with vertical background shear to generate strong barotropic anomalies near the heating source, and what weak anomalies do exist don't overlap with the barotropic background wind to radiate barotropic teleconnections.

In short, two factors (the amplitude and latitudinal position of the subtropical jet) could explain why the ENSO teleconnections are enhanced in the winter hemisphere and almost absent in the summer hemisphere (Fig. 7). Is the summer hemispheric subtropical jet too weak, or too far from the heating latitude? To answer this question, we perform four model experiments as summarized in Table 3. In these experiments, the background states are idealized using a Gaussian function:

$$(\bar{U}, \hat{U}) = (\bar{U}_o, \hat{U}_o) \exp \left[- \left(\frac{\theta - \theta_o}{20^\circ} \right)^2 \right]. \quad (28)$$

As shown in Fig. 8, the background flow for Case-7 ($\bar{U}_o = 30 \text{ ms}^{-1}$; $\hat{U}_o = -15 \text{ ms}^{-1}$; $\theta_o = 30^\circ\text{N}$) represents that of the winter hemisphere (i.e., DJF in the northern hemisphere), whereas the background flow for Case-10 ($\bar{U}_o = 20 \text{ ms}^{-1}$; $\hat{U}_o = -10 \text{ ms}^{-1}$; $\theta_o = 45^\circ\text{N}$) represents that of the summer hemisphere (i.e., JJA in the southern hemisphere). The background flow for Case-8 is identical to that of the Case-10 (summer hemispheric condition) except that it is centered at $\theta_o = 30^\circ\text{N}$, whereas the background flow for Case-9 is identical to that of the Case-7 (winter hemispheric condition) except that it is centered at $\theta_o = 45^\circ\text{N}$.

Figure 9 shows the barotropic stream function and rotational wind anomalies for (a) Case-7, (b) Case-8 and (c) Case-9. The model solutions for the Case-7 capture reasonably well the barotropic teleconnections into the winter hemisphere shown in Fig. 7. More importantly, when the amplitude of background flow is reduced to that of the summer hemisphere (Case-8), barotropic wind anomalies are still excited and transmitted to high latitudes. The amplitude and wavelength of the barotropic flow anomalies are smaller in Case-8 than in Case-7 because the barotropic background wind is weaker in Case-8 (see (25) for why the wavelength should decrease as \bar{U} decreases). Nevertheless, this model result suggests that the summer hemispheric background flow is strong enough to host barotropic stationary Rossby waves. On the other hand, almost no barotropic signals are generated in the Case-9 although the background flow in this case is as strong as that of the winter hemisphere (Case-7). It is apparent that the vertical background shear in this case is centered too far off from the tropics to interact with the heat-driven baroclinic anomalies, which are confined in the tropics, and thus barotropic flow

anomalies are not generated. Case-10 is not shown because almost no barotropic signals are generated in that case.

In summary, our model results suggest that the ENSO teleconnections are enhanced in the winter hemisphere mainly because the summer hemispheric subtropical jet is too far from the heating source. However, if the heating source is specified in the vicinity of the jet, stationary Rossby waves can be still excited in the summer hemisphere. One example involving such waves is the East Asian monsoon in boreal summer: Sardeshmukh and Hoskins (1988) showed that diabatic heating (centered around 110°E and 20°N) associated with the East Asian summer monsoon can generate stationary Rossby waves spanning the entire Northern hemisphere.

Another example is the summer onset of the Atlantic warm pool (AWP) over the Gulf of Mexico and Caribbean Sea (Wang and Enfield 2001). Wang et al. (2007) showed that the summer onset of the AWP forces a classical Gill-type response in the troposphere. Since SST over the AWP is maximized around 90°W and 25°N in JJA, our model results suggest that AWP-induced diabatic heating should trigger teleconnections into high latitudes. Figures 10a and 11a show the baroclinic and barotropic stream function anomalies in JJA reproduced from the NCAR Community Atmospheric Model (CAM3) experiments of Wang et al. (2007). These plots show the difference between CAM3 ensemble runs with and without the AWP, representing the net impact by the summer onset of the AWP. As expected, a Gill-type baroclinic response (Wang et al. 2007) interacts with the vertical background shear to force barotropic flow anomalies near the heating source. Then, the barotropic background wind in JJA allows these barotropic stationary Rossby waves to emanate from the AWP region to the high latitudes (Fig. 11a). We attempt to replicate these CAM3 results of Wang et al. (2007) by forcing our model with an idealized heating source specified over the AWP region. The heating source is the same as (24) except that

θ is now replaced with $\theta - 25^\circ$ and λ_0 is set to 90°W . The JJA basic state is obtained by using the stream functions at 250 and 750mb from the monthly NCAR-NCEP reanalysis - the basic states are not zonally averaged in this case. As shown in Fig. 10b and Fig. 11b, our simple model reasonably well simulates the CAM3 results over the North Atlantic regions, confirming that the summer onset of the AWP may have a remote influence on the North American and European summer climate and also on the air-sea interaction over the high-latitude North Atlantic. We repeated the same model experiment but with the zonally averaged (over 90°W - 0°) JJA basic states, and found very similar model solutions (not shown).

5. Summary and discussion

The main objective of this study was to build, test, and document a minimal complexity model capable of simulating both the local and teleconnection responses to tropical heating anomalies. A two-mode (barotropic and baroclinic) model was shown to capture three fundamental dynamic processes: 1) a heat-induced baroclinic mode as described by the Matsuno-Gill model (Gill 1980); 2) a barotropic Rossby wave source resulting from conversion of the heat-induced baroclinic mode into barotropic anomalies; and 3) barotropic teleconnections to high latitudes, as in the barotropic stationary wave model of Branstator (1983). Solutions linearized about some idealized and realistic basic states showed that background vertical wind shear plays an important role in converting energy from the heat-induced baroclinic flow anomalies into barotropic motions near the heating source, consistent with the findings of Kasahara and Silva Dias (1986) and Wang and Xie (1996). These barotropic flow anomalies in turn interact with the depth-independent background westerly wind to transmit the barotropic

signals to high latitudes and other ocean basins. Both baroclinic and barotropic background wind fields are therefore required for tropical heating to radiate barotropic teleconnections to high latitudes.

We also found that the baroclinic solution components are confined within the tropics and largely insensitive to the background wind fields. This result suggests that the feedback from barotropic to baroclinic motions is weak. Based on the dispersion relationship for baroclinic Rossby wave, baroclinic Rossby waves propagate too slowly to become stationary in middle and high latitudes. Based on these results, we conclude that the original Matsuno-Gill model largely captures the heat-induced baroclinic response, provided that the parameter values used in this study are realistic.

In the tropics, the heat-induced barotropic response has the form of an anticyclonic vortex pair to the north and south of the heating source. When superposed on the heat-induced baroclinic response, this opposes the baroclinic cyclonic vortex pair in the lower troposphere and reinforces the anticyclonic vortex pair in the upper level. This appears to explain why El Niño is associated with a strong anticyclone pair in the upper troposphere and a relatively weak cyclone pair in the lower troposphere.

When the model is linearized about realistic basic states for boreal winter (DJF) and summer (JJA), it successfully reproduces the hemispheric asymmetry of ENSO teleconnections. Further experiments suggest that the ENSO teleconnections are enhanced in the winter hemisphere mainly because the summer hemispheric subtropical jet is too far from the heating source. Still, the summer hemispheric subtropical jet can host robust stationary Rossby waves if heating occurs in the vicinity of the jet. Based on this finding and the previous AGCM study by Wang et

al. (2007), we show that the summer latent heating over the AWP can have a profound impact on the North American and European summer climate.

Although not shown here, we also forced the model with an observed El Niño heating anomaly in realistic DJF background wind fields. The barotropic cyclonic wind anomalies over the North Pacific and the Walker-circulation anomalies over the equatorial Pacific were reasonably well reproduced (not shown). However, the model also produces some unrealistic signals, such as a too-strong subsidence over the western equatorial Pacific and the Amazon regions. These errors are partly due to the oversimplifications in the horizontal and vertical structure of the diabatic heating anomaly and background mean flow (Sardeshmukh and Hoskins 1988; Ting and Sardeshmukh 1993). It is also important to point that our model does not include the vorticity flux by transient synoptic eddies, which is known to be important in the maintenance of the mid-latitude response to ENSO (Kok and Opsteegh 1985; Held et al. 1989). Additionally, it must be recognized that the heat-induced mid-latitude response does contain a baroclinic component, although in much smaller amplitude than in the tropics. Thus, it is possible that the weak temperature gradient approximation, which is used in deriving the equation for baroclinic geopotential, may incorrectly simulate the baroclinic response in mid-latitudes. Yet another source of model errors originates from the lack of a frictional boundary layer, where Ekman divergence due to the baroclinic cyclones and anticyclones in the lower level can excite a barotropic response. Explicit considerations of these missing mechanisms and further model improvements are left for future study.

Although the current model has difficulty in reproducing some of the observed features associated with El Niño, it seems the simplest system that can explain both the local and teleconnection responses to tropical heating anomalies, and thus may be a useful addition to the

model hierarchy, as a tool to increase our understanding of heat-induced global atmospheric circulations. Potential applications include a coupling of this model with a reduced gravity ocean model, to extend the El Niño model of Zebiak and Cane (1987) in latitude. Such a coupled model may help elucidate global atmosphere-ocean dynamic processes associated with El Niño, beyond traditional tropical atmosphere-ocean feedbacks.

Acknowledgements. We would like to thank Grant Branstator at NCAR for kindly providing us with his barotropic vorticity equation solver, which was very helpful for developing the numerical code for our work. We also wish to thank David Enfield, David Straus, and two anonymous reviewers for thoughtful comments and suggestions, which led to a significant improvement of the paper. This work was supported by a grant from National Oceanic and Atmospheric Administration (NOAA) Climate Program Office and by the base funding of NOAA Atlantic Oceanographic and Meteorological Laboratory (AOML). The findings and conclusions in this report are those of the authors and do not necessarily represent the views of the funding agency.

References

- Adams, J. C. and P. N. Swarztrauber, 1999: SPHEREPACK 3.0: A model development facility. *Mon. Wea. Rev.*, 127, 1872-1878.
- Branstator, G., 1983: Horizontal energy propagation in a barotropic atmosphere with meridional and zonal structure. *J. Atmos. Sci.*, 40, 1689-1708.
- Branstator, G., 1990: Low-frequency patterns induced by stationary waves. *J. Atmos. Sci.*, 47, 629-648.
- Bourke, W., 1972: An efficient, on-level, primitive equation spectral model. *Mon. Wea. Rev.*, 100, 683-689.
- Davey, M. K. and A. E. Gill, 1987: Experiments on tropical circulation with a simple moist model. *Quart. J. Roy. Meteor. Soc.*, 113, 1237-1269.

- Gill, A. E., 1980: Some simple solutions for heat-induced tropical circulation. *Quart. J. Roy. Meteor. Soc.*, 106, 447–462.
- Grose, W. L. and B. J. Hoskins, 1979: On the influence of orography on large-scale atmospheric flow. *J. Atmos. Sci.*, 36, 223–234.
- Held, I. M. and M. J. Suarez, 1978: A two-level primitive equation atmospheric model designed for climatic sensitivity experiments. *J. Atmos. Sci.*, 35, 206–229.
- Held, I. M., S. W. Lyons, and S. Nigam, 1989: Transients and the extratropical response to El Niño. *J. Atmos. Sci.*, 46, 163–174.
- Holton, J. R., 1992: An introduction to dynamic meteorology. Academic Press, 3rd Ed. San Diego, 511 pp.
- Horel, J. D. and J. M. Wallace, 1981. Planetary-scale atmospheric phenomena associated with the South Oscillation. *Mon. Wea. Rev.*, 109, 813–829.
- Hoskins, B. J. and A. J. Simmons, 1975: A multi-layer spectral model and the semi-implicit method. *Quart. J. Roy. Meteor. Soc.*, 103, 553–567.
- Hoskins, B. J. and D. J. Karoly, 1981: The steady linear response of a spherical atmospheric thermal and orographic forcing. *J. Atmos. Sci.*, 38, 1179–1196.
- Jin, F.-F. and B. J. Hoskins, 1995: The direct response to tropical heating in a baroclinic atmosphere. *J. Atmos. Sci.*, 52, 307–319.
- Kalnay, E., M. Kanamitsu, R. Kistler, W. Collins, D. Deaven, L. Gandin, M. Iredell, S. Saha, G. White, J. Woollen, Y. Zhu, M. Chelliah, W. Ebisuzaki, W. Higgins, J. Janowiak, K. C. Mo, C. Ropelewski, J. Wang, Leetmaa, R. Reynolds, R. Jenne, and D. Joseph, 1996: The NCEP/NCAR 40-year Reanalysis Project. *Bull. American Meteorol. Soc.*, 77, 437–471.
- Kasahara, A. and P. L. da Silva Dias, 1986: Response of planetary waves to stationary tropical heating in a global atmosphere with meridional and vertical shear. *J. Atmos. Sci.*, 43, 1893–1911.
- Kleeman, R., 1989: A modeling study of the effect of the Andes on the summertime circulation of tropical South America. *J. Atmos. Sci.*, 46, 3344–3362.
- Klein, S. A., B. J. Soden and N.-C. Lau, 1999: Remote sea surface temperature variations during ENSO: evidence for a tropical atmospheric bridge. *J. Climate*, 12, 917–932.
- Kok, C. J., and J. D. Opsteegh, 1985: On the possible causes of anomalies in seasonal mean circulation patterns during the 1982–83 El Niño event. *J. Atmos. Sci.*, 42, 677–694.
- Lau, N.-C., 1981: A diagnostic study of recurrent meteorological anomalies appearing in a 15-year simulation with a GFDL general circulation model. *Mon. Wea. Rev.*, 109, 2287–2311.
- Lin J. L., B. E. Mapes, and W. Han, 2008: What are the sources of mechanical dampings in Matsuno-Gill models? *J. Climate*, 21, 165–179.
- Matsuno, T., 1966: Quasi-geostrophic motions in the equatorial area. *J. Meteor. Soc. Japan*, 44, 25–43.
- Navarra, A., W. F. Stern, and K. Miyakoda, 1994: Reduction of the Gibbs oscillation in spectral model simulations. *J. Climate*, 7, 1169–1183.
- Neelin, J. D., 1988: A simple model for surface stress and low-level flow in the tropical atmosphere driven by prescribed heating. *Quart. J. Roy. Meteor. Soc.*, 114, 747–770.
- Pexoto, J. P. and A. H. Oort, 1992: Physics of climate. American Institute of Physics, New York, 520p.
- Robert, A. J., 1966: The integration of a low order spectral form of primitive meteorological equations. *J. Meteor. Soc. Japan*, 44, 237–245.

- Sardeshmukh P. D. and B. J. Hoskins, 1988: The generation of global rotational flow by steady idealized tropical divergence. *J. Atmos. Sci.*, 45, 1228-1251.
- Schopf, P. S. And M. J. Suarez, 1988: Vacillations in a coupled ocean-atmosphere model. *J. Atmos. Sci.*, 45, 549-566.
- Straus, D. M., S. Corti and F. Molteni, 2007: Circulation regimes: chaotic variability versus SST-forced predictability. *J. Climate*, 20, 2251-2272.
- Ting, M. and I. M. Held, 1990: The stationary wave response to tropical SST anomaly in an idealized GCM. *J. Atmos. Sci.*, 47, 2546-2566.
- Ting, M. and P. D. Sardeshmuku, 1993: Factors determining the extratropical response to equatorial diabatic heating anomalies. *J. Atmos. Sci.*, 50, 907-918.
- Wallace, J. M. and D. S. Gutzler, 1981: Teleconnections in the geopotential height field during the northern hemispheric winter. *Mon. Wea. Rev.*, 109, 784-812.
- Wang, B. and T. Li, 1993: A simple tropical atmosphere model of relevance to short-term climate variations. *J. Atmos. Sci.*, 50, 260-284.
- Wang, B. and X. Xie, 1996: Low-frequency equatorial waves in vertically sheared zonal flow. Part I: stable waves. *J. Atmos. Sci.*, 53, 449-467.
- Wang, C., and D. B. Enfield, 2001: The tropical Western Hemisphere warm pool. *Geophys. Res. Lett.*, 28, 1635-1638.
- Wang, C., S.-K. Lee, and D. B. Enfield, 2007: Impact of the Atlantic warm pool on the summer climate of the Western Hemisphere. *J. Climate*, 20, 5021-5040.
- Watanabe, M. and M. Kimoto, 2000: Atmosphere-ocean thermal coupling in the North Atlantic: a positive feedback. *Quart. J. Roy. Meteor. Soc.*, 126, 3343-3369.
- Watanabe, M. and F.-F. Jin, 2003: A moist linear baroclinic model: coupled dynamical-convective response to El Niño. *J. Climate*, 16, 1121-1139.
- Webster, P. J., 1981: Mechanisms determining the atmospheric response to sea surface temperature anomalies. *J. Atmos. Sci.*, 38, 554-571.
- Zebiak, S., 1986: Atmospheric convergence feedback in a simple model for El Niño. *Mon. Wea. Rev.*, 114, 1263-1271.
- Zebiak, S. And M. A. Cane, 1987: A model El Niño-Southern Oscillation. *Mon. Wea. Rev.* 115, 2262-2278.

Table 1. Prescribed idealized basic states for Case-1, 2, 3, and 4

Experiment	Description	Background zonal wind speed (m s^{-1})
Case-1	No background flow	$\bar{U} = 0$; $\hat{U} = 0$
Case-2	Barotropic background flow	$\bar{U} = 25 \cos\theta$; $\hat{U} = 0$
Case-3	Baroclinic background flow	$\bar{U} = 0$; $\hat{U} = -15 \cos\theta$
Case-4	Barotropic and baroclinic background flow	$\bar{U} = 25 \cos\theta$; $\hat{U} = -15 \cos\theta$

Table 2. Prescribed realistic basic states for Case-5 and 6 (NCEP-NCAR reanalysis) as shown in Fig. 6.

Experiment	Description
Case-5	Background zonal wind of DJF averaged over 120°E-100°W
Case-6	Background zonal wind of JJA averaged over 120°E-100°W

Table 3. Prescribed idealized basic states for Case-7, 8, 9, and 10 as shown in Fig. 8.

Experiment	Description	Background zonal wind speed (m s^{-1}) and θ_o
Case-7	Idealized basic state for DJF	$\bar{U}_o = 30$; $\hat{U}_o = -15$; $\theta_o = 30^\circ\text{N}$
Case-8	\bar{U}_o , \hat{U}_o for JJA and θ_o for DJF	$\bar{U}_o = 20$; $\hat{U}_o = -10$; $\theta_o = 30^\circ\text{N}$
Case-9	\bar{U}_o , \hat{U}_o for DJF and θ_o for JJA	$\bar{U}_o = 30$; $\hat{U}_o = -15$; $\theta_o = 45^\circ\text{N}$
Case-10	Idealized basic state for JJA	$\bar{U}_o = 20$; $\hat{U}_o = -10$; $\theta_o = 45^\circ\text{N}$

Figure Captions

Figure 1. Baroclinic geopotential and wind (vector plot) anomalies for (a) Case-1 (no background flow) and (b) Case-2 (barotropic background flow). Negative contour lines are dashed. Contour interval is $50 \text{ m}^2 \text{ s}^{-2}$ for both (a) and (b).

Figure 2. Same as Figure 1, but for baroclinic stream function and rotational wind (vector plot) anomalies. Contour interval is $10^6 \text{ m}^2 \text{ s}^{-1}$ for both (a) and (b).

Figure 3. Same as Figure 1, but for baroclinic velocity potential and divergent wind (vector plot) anomalies. Contour interval is $10^6 \text{ m}^2 \text{ s}^{-1}$ for both (a) and (b).

Figure 4. Barotropic stream function and wind (vector plot) anomalies for (a) Case-3 (baroclinic background flow) and (b) Case-4 (barotropic and baroclinic background flow). Negative contour lines are dashed. Contour interval is $10^6 \text{ m}^2 \text{ s}^{-1}$ for both (a) and (b).

Figure 5. Case-3 (baroclinic background flow): Stream function and rotational wind (vector plot) for (a) the upper level (250 mb) and (b) the lower level (750 mb). Negative contour lines are dashed. Contour interval is $1.5 \times 10^6 \text{ m}^2 \text{ s}^{-1}$ for both (a) and (b).

Figure 6. Climatological boreal winter (DJF: solid lines) and summer (JJA: dashed lines) zonal winds for (a) barotropic and (b) baroclinic components, both zonally averaged for the longitude band of 120°E - 100°W and obtained from the NCAR-NCEP reanalysis.

Figure 7. Barotropic stream function and wind (vector plot) anomalies for (a) Case-5 (DJF) and (b) Case-6 (JJA). Negative contour lines are dashed. Contour interval is $10^6 \text{ m}^2 \text{ s}^{-1}$ for both (a) and (b).

Figure 8. Idealized zonal background winds for Case-7, Case-8, Case-9 and Case-10: (a) barotropic and (b) baroclinic components.

Figure 9. Barotropic stream function and wind (vector plot) anomalies for (a) Case-7, (b) Case-8, and (c) Case-9. Negative contour lines are dashed. Contour interval is $10^6 \text{ m}^2 \text{ s}^{-1}$ for all cases.

Figure 10. Baroclinic stream function: (a) the difference between the CAM3 runs with and without AWP in JJA reproduced from Wang et al. (2007); (b) Case-11 (AWP). Contour interval is $1.0 \times 10^6 \text{ m}^2 \text{ s}^{-1}$ for (a) and $2.0 \times 10^6 \text{ m}^2 \text{ s}^{-1}$ for (b).

Figure 11. Barotropic stream function: (a) the difference between the CAM3 runs with and without AWP in JJA reproduced from Wang et al. (2007); (b) Case-11 (AWP). Contour interval is $1.0 \times 10^6 \text{ m}^2 \text{ s}^{-1}$ for (a) and $0.5 \times 10^6 \text{ m}^2 \text{ s}^{-1}$ for (b).

Baroclinic Geopotential & Wind

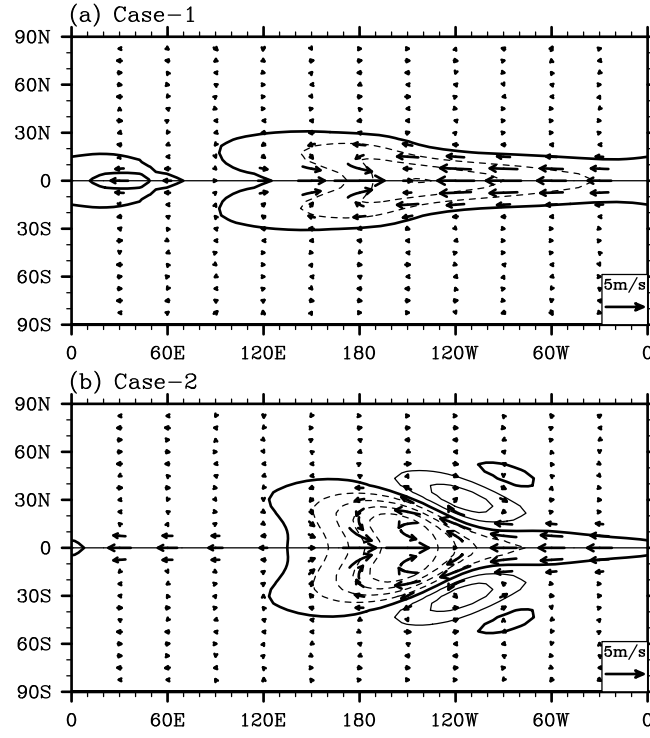


Figure 1. Baroclinic geopotential and wind (vector plot) anomalies for (a) Case-1 and (b) Case-2. Negative contour lines are dashed. Contour interval is $50 \text{ m}^2 \text{ s}^{-2}$ for both (a) and (b).

Baroclinic Stream Function & Rotational Wind

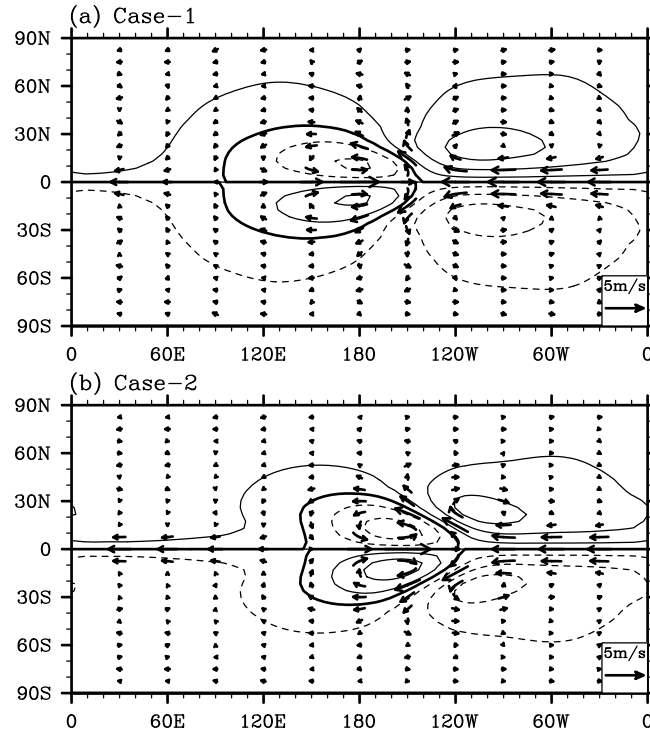


Figure 2. Same as Figure 1, but for baroclinic stream function and rotational wind (vector plot) anomalies. Contour interval is $10^6 \text{ m}^2 \text{ s}^{-1}$ for both (a) and (b).

Baroclinic Velocity Potential & Divergent Wind

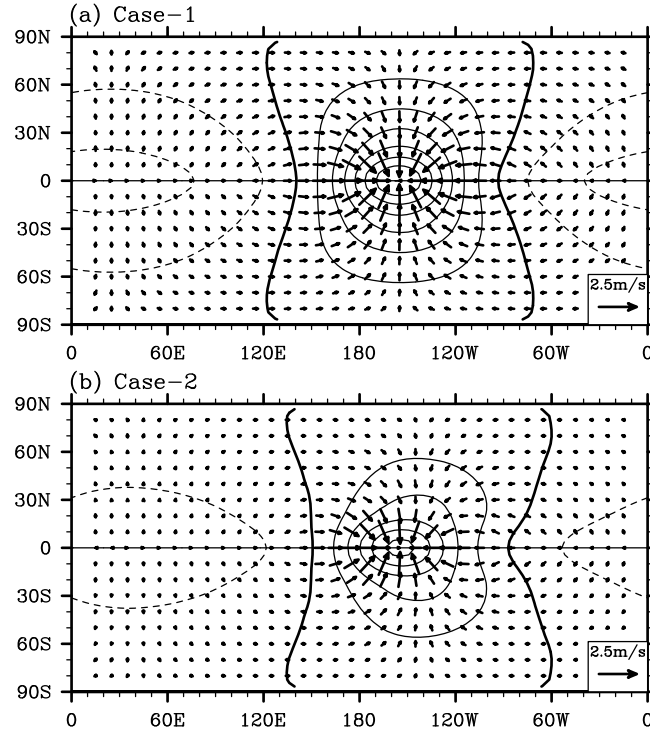


Figure 3. Same as Figure 1, but for baroclinic velocity potential and divergent wind (vector plot) anomalies. Contour interval is $10^6 \text{ m}^2 \text{ s}^{-1}$ for both (a) and (b).

Barotropic Stream Function & Rotational Wind

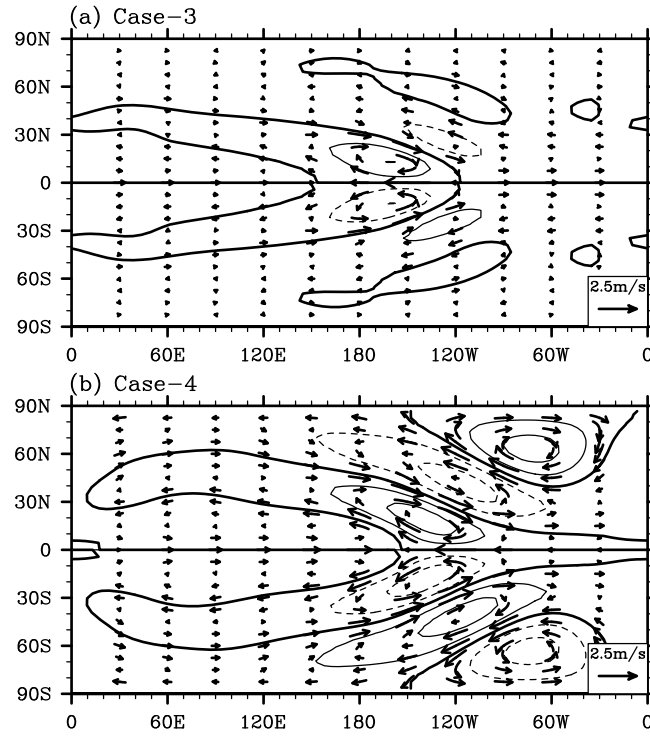


Figure 4. Barotropic stream function and wind (vector plot) anomalies for (a) Case-3 and (b) Case-4. Negative contour lines are dashed. Contour interval is $10^6 \text{ m}^2 \text{ s}^{-1}$ for both (a) and (b).

Case-3: Stream Function & Rotational Wind

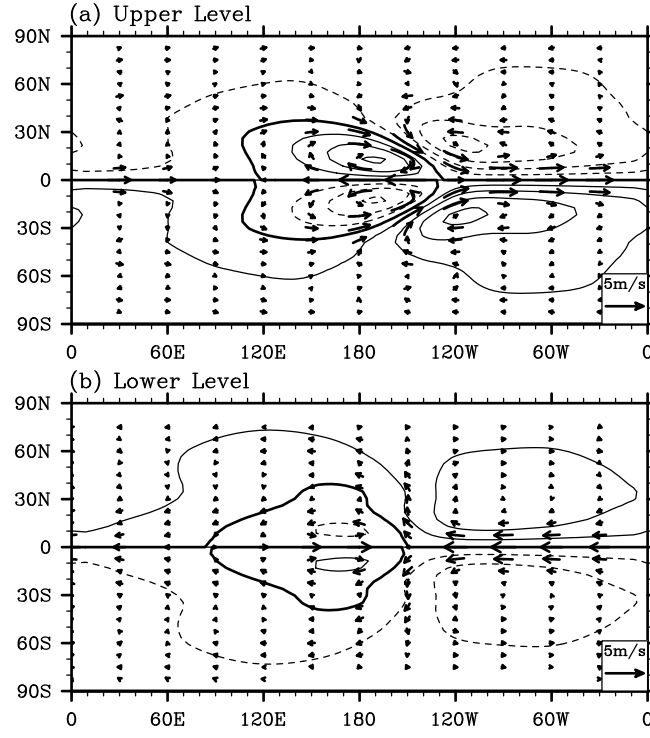


Figure 5. Case-3: Stream function and rotational wind (vector plot) for (a) the upper level (250 mb) and (b) the lower level (750 mb). Negative contour lines are dashed. Contour interval is $1.5 \times 10^6 \text{ m}^2 \text{ s}^{-1}$ for both (a) and (b).

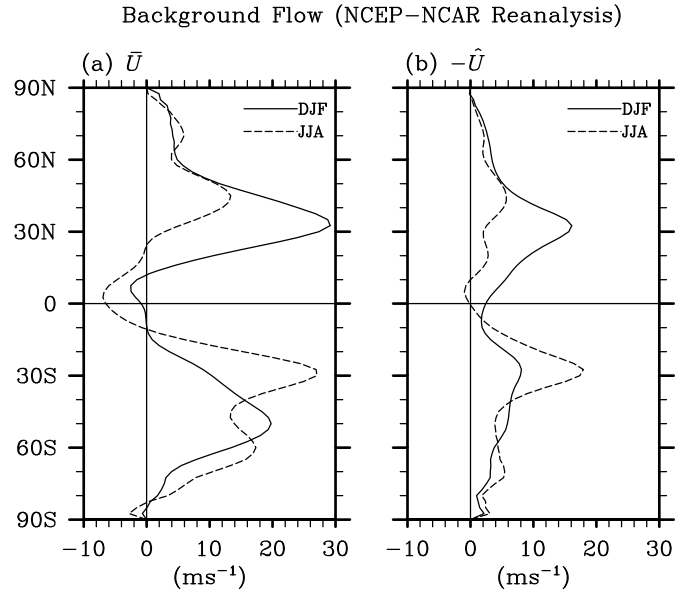


Figure 6. Climatological boreal winter (DJF: solid lines) and summer (JJA: dashed lines) zonal winds for (a) barotropic and (b) baroclinic components, both zonally averaged for the longitude band of 120°E–100°W and obtained from the NCAR–NCEP reanalysis.

Barotropic Stream Function & Rotational Wind

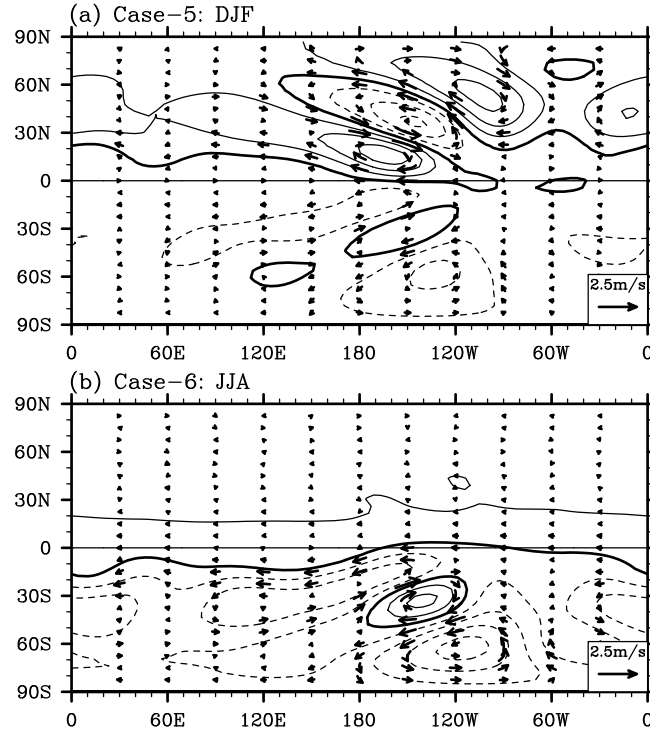


Figure 7. Barotropic stream function and wind (vector plot) anomalies for (a) Case-5 (DJF) and (b) Case-6 (JJA). Negative contour lines are dashed. Contour interval is $10^6 \text{ m}^2 \text{ s}^{-1}$ for both (a) and (b).

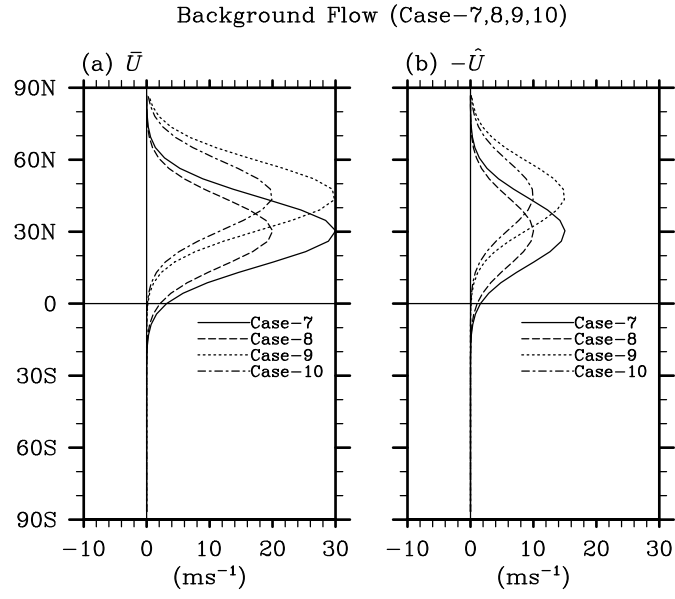


Figure 8. Idealized zonal background winds for Case-7, Case-8, Case-9 and Case-10: (a) barotropic and (b) baroclinic components.

Barotropic Stream Function & Rotational Wind

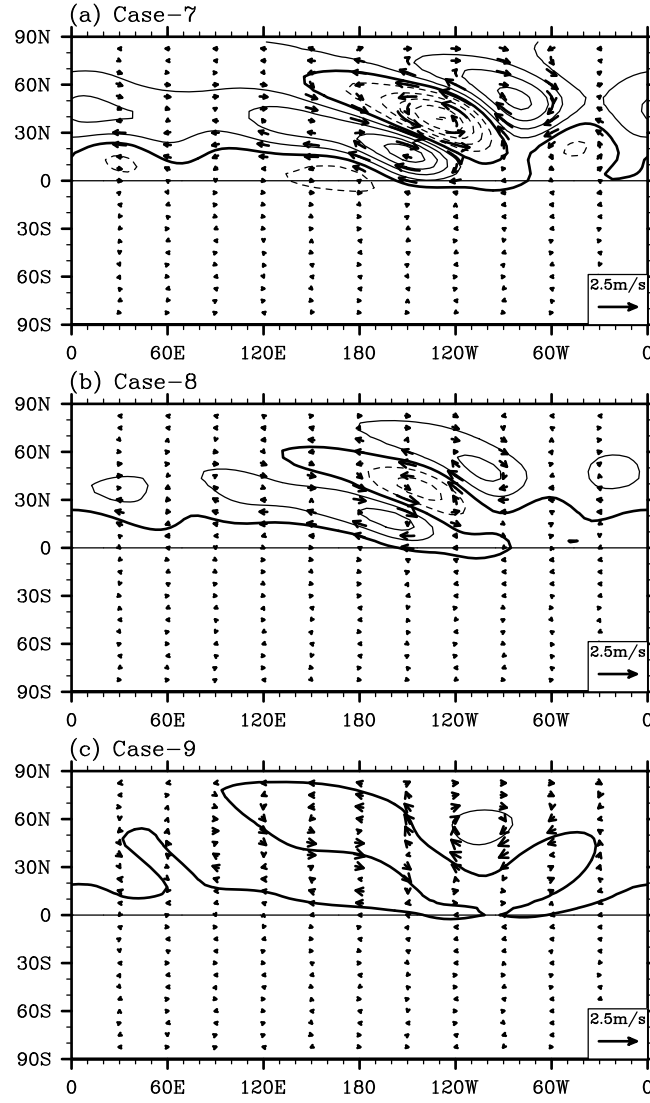


Figure 9. Barotropic stream function and wind (vector plot) anomalies for (a) Case-7, (b) Case-8, and (c) Case-9. Negative contour lines are dashed. Contour interval is $10^6 \text{ m}^2 \text{ s}^{-1}$ for all cases.

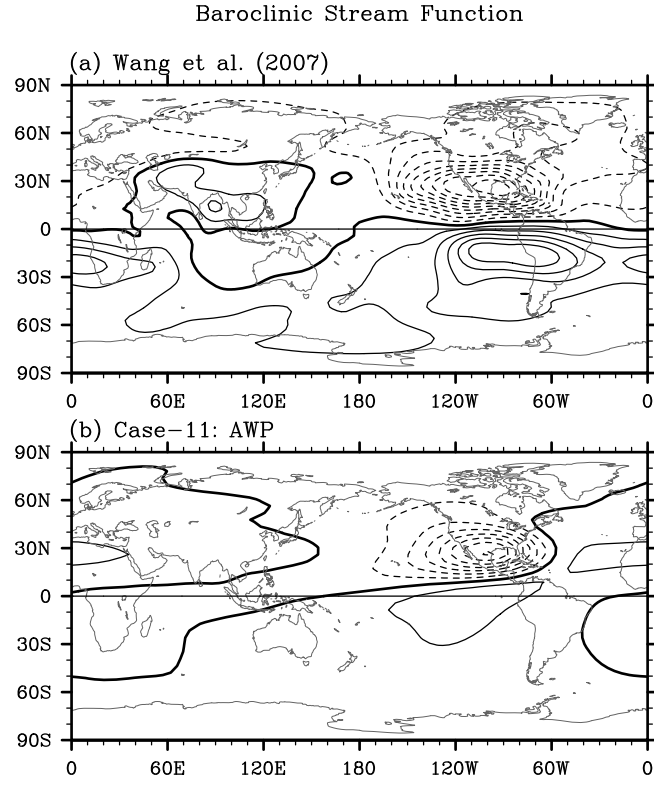


Figure 10. Baroclinic stream function: (a) the difference between the CAM3 runs with and without AWP in JJA reproduced from Wang et al. (2007); (b) Case-11 (AWP). Contour interval is $1.0 \times 10^6 \text{ m}^2 \text{ s}^{-1}$ for (a) and $2.0 \times 10^6 \text{ m}^2 \text{ s}^{-1}$ for (b).

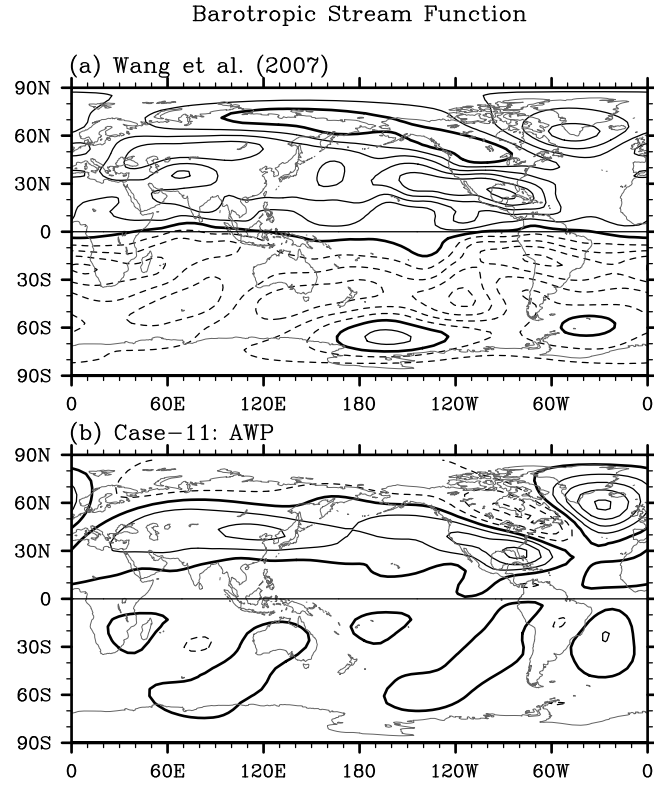


Figure 11. Barotropic stream function: (a) the difference between the CAM3 runs with and without AWP in JJA reproduced from Wang et al. (2007); (b) Case-11 (AWP). Contour interval is $1.0 \times 10^6 \text{ m}^2 \text{ s}^{-1}$ for (a) and $0.5 \times 10^6 \text{ m}^2 \text{ s}^{-1}$ for (b).